Inorganic Chemistry

Article

pubs.acs.org/IC

Synthesis, Crystal Structure, and Solid-State NMR Investigations of Heteronuclear Zn/Co Coordination Networks — A Comparative Study

Anusree Viswanath Kuttatheyil,[†] Daniel Lässig,[‡] Jörg Lincke,[‡] Merten Kobalz,[‡] Maria Baias,[§] Katja König,[∥] Jörg Hofmann,[∥] Harald Krautscheid,[‡] Chris J. Pickard,[⊥] Jürgen Haase,[†] and Marko Bertmer*[,†]

[†]Universität Leipzig, Fakultät für Physik und Geowissenschaften, Linnéstr. 5, D-04103, Germany

[‡]Universität Leipzig, Fakultät für Chemie und Mineralogie, Johannisallee 29, D-04103, Germany

[§]Universitè de Lyon, Centre de RMN à très hauts champs, CNRS/ENS Lyon/UCBL, 5 Rue de la Doua, 69100 Villeurbanne, France

[∥]Institut für Nichtklassische Chemie e. V., Permoserstr.15, D-04318, Germany

[⊥]Department of Physics & Astronomy, University College London, Gower Street, London, United Kingdom

Supporting Information

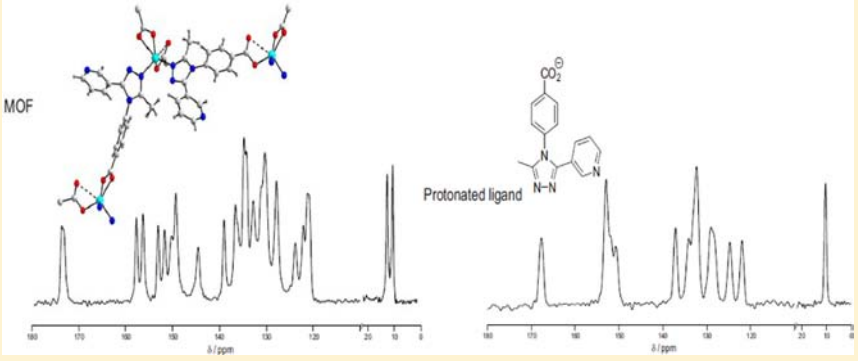

ABSTRACT: Synthesis and solid-state NMR characterization of two isomorphous series of zinc and cobalt coordination networks with 1,2,4-triazolyl benzoate ligands are reported. Both series consist of 3D diamondoid networks with four-fold interpenetration. Solid-state NMR identifies the metal coordination of the ligands, and assignment of all ^{1}H and ^{13}C shifts was enabled by the combination of ^{13}C editing, FSLG-HETCOR spectra, and 2D $^{1}H-^{1}H$ back-to-back (BABA) spectra with results from NMR-CASTEP calculations. The incorporation of Co^{2+} replacing Zn^{2+} ions in the MOF over the full range of concentrations has significant influences on the NMR spectra. A uniform distribution of metal ions is documented based on the analysis of ^{1}H T_1 relaxation time measurements.

INTRODUCTION

Coordination networks or often called metal−organic frameworks (MOFs) have attracted tremendous attention in recent years as a new class of porous compounds.[1,2] The dramatic increase in the number of publications in this area shows its growing interest as can be seen for instance in two reviews.[3,4] The wide structural diversity offered by this class has high potential for various applications, including gas storage,[5,6] catalysis,[7] sensoring,[8] gas separation,[9] and others, such as heat-transformation applications.[10−13] They are designed from inorganic building blocks, for example, metal ions or clusters interconnected by polyfunctional organic ligands.

Carboxylates are the most extensively studied polyfunctional organic ligands. Apart from this, ligands having a combination of both neutral donor groups, such as pyridine or 1,2,4-triazoles, and anionic functional groups, such as carboxylates, are of interest[14,15] where the coordination properties of both functional groups can be combined. 1,2,4-Triazole derived ligands show promising coordination chemistry especially when substituted with certain donor groups. The synthesis of such ligands has been reported[16] and successfully applied for the preparation of novel MOFs.[17,18] Especially MOFs with N-donor ligands show interesting properties for heterogeneous catalysis.[19] On the basis of the ligands (**L1**$^{-}$) (Me-3py-trz-pba)$^{-}$ and (**L2**$^{-}$) (Me$_2$trz-pba)$^{-}$ (shown in Scheme 1; the corresponding structural motifs of the coordination polymers are given in **1**(b) and **2**(b), respectively), we analyzed two Zn based MOFs (**1** and **2**, structures included in Scheme 1). Additionally, we also studied mixed metal MOFs (heteronuclear MOFs) $^{3}_{\infty}[Zn_{1-x}Co_x(L)_2]$ (Series I and Series II) using these ligands, combining metal ions of different electron configurations. Such mixed-metal systems exhibit interesting catalytic properties.[19] The heteronuclear MOFs were prepared

Received: December 3, 2012
Published: April 1, 2013

   dx.doi.org/10.1021/ic302643w | *Inorg. Chem.* 2013, 52, 4431−4442

Scheme 1. Ligand Structures of 1(a) L1$^-$ (Me-3py-trz-pba)$^-$ and 2(a) L2$^-$ (Me$_2$trz-pba)$^-$ with Carbon Numbering Used in This Text. The Corresponding Structural Motifs of the Coordination Polymers are Given in 1(b) and 2(b), Respectively

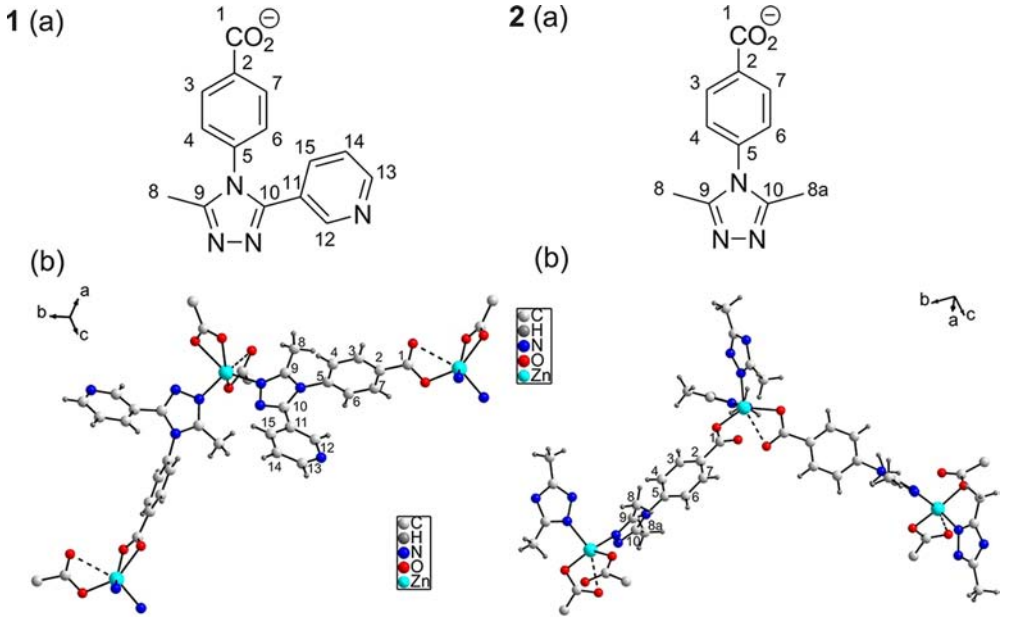

by partially substituting the diamagnetic Zn^{2+} ions with varying amounts of paramagnetic Co^{2+} ions in the full range from x = 0.02 to x = 1.

Various experimental methods can be used for the structural characterization of porous coordination compounds. A better understanding of the various interactions present in the metal–ligand framework is inevitable to explore its potential applicability. Solid-state NMR is a versatile tool for studying the different interactions present in porous coordination frameworks, which is increasingly used for the characterization of structure and dynamics in these materials.[20−24] NMR spectra of solid samples provide information on the detailed local electronic structure of each nucleus reflected as a chemical shift without the need of long-range order. Therefore, noncrystalline materials can be characterized with solid-state NMR, which is increasingly used for the characterization of structure and dynamics in these materials.[25−27] Furthermore, using this method, it is easy to determine the presence of small mobile molecules, while X-ray analysis is more complicated or impossible.[28]

In this paper, we report on the synthesis and detailed structural elucidation of two Zn MOFs together with their corresponding protonated ligands by means of X-ray structure analysis, ^{1}H and ^{13}C solid-state NMR, and quantum chemical calculations. Detailed assignments of NMR resonances were done, including the changes in individual chemical shifts with respect to the protonated ligands. Full resonance assignments were achieved with frequency switched Lee–Goldburg (FSLG) heteronuclear ^{1}H–^{13}C correlation experiments (HETCOR)[29] and ^{1}H–^{1}H homonuclear correlation experiments using the back-to-back (BABA)[30] sequence. Our experimental results were complemented by DFT calculations of NMR parameters, using the GIPAW method[31] implemented in the CASTEP code,[32] which has already been proven to be a reliable tool in characterizing the NMR properties of crystalline solids.[33−40]

Heteronuclear MOFs with varying percentages of paramagnetic Co^{2+} were also investigated with ^{1}H and ^{13}C NMR to study the influence of paramagnetic metal ions on the parent framework. In order to gain information about the distribution of Co^{2+} in the MOF network, an analysis of ^{1}H T_1 relaxation times was performed.

EXPERIMENTAL SECTION

Synthesis. The synthesis of the respective N-donor ligands was previously reported by Lässig et al.[16] While the synthesis and characterization of the coordination polymers $^3_\infty$[M(Me-3py-trz-pba)$_2$] (M = Zn: **1**, Zn/Co: Series I) were reported earlier,[17] herein, we present the structurally related system $^3_\infty$[Zn(Me$_2$trz-pba)$_2$] (**2**) with the dimethylated ligand (Me$_2$trz-pba)$^-$. Multigram amounts of MOFs of the two isomorphous series were obtained by heating the starting materials, that is, Zn(OAc)$_2$·2H$_2$O and the respective protonated ligands H(Me-3py-trz-pba) and H(Me$_2$trz-pba) under reflux in DMF for 48 h. Afterwards, the reaction mixtures were cooled to room temperature, and the solid products were washed with DMF and ethanol, yielding fine microcrystalline powders after drying in air. The IR, thermogravimetric and PXRD data of **1** and **2** are given in the Supporting Information or can be found in the respective publication.[17]

For the preparation of mixed Zn/Co MOFs of type $^3_\infty$[Zn$_{1-x}$Co$_x$(Me-3py-trz-pba)$_2$] (Series I), Zn(OAc)$_2$·2H$_2$O was partially replaced by 5, 10, 20, 25, 30, 40, 50 and 75% of CoCl$_2$·6H$_2$O, respectively. Similarly, for the preparation of mixed Zn/Co MOFs of type $^3_\infty$[Zn$_{1-x}$Co$_x$(Me$_2$trz-pba)$_2$]·DMF·1.5·H$_2$O (Series II), Zn(OAc)$_2$·2H$_2$O was partially replaced by 2, 5, 10, 25, 50 and 75% of CoCl$_2$·6H$_2$O, respectively. For both series, also samples with only cobalt as a metal connector were prepared as well.

To determine the actual amounts of zinc and cobalt incorporated into the MOFs, atomic absorption spectroscopy (AAS) was carried out. For this, the samples were first incinerated and afterwards dissolved in nitric acid. Experiments were performed using a Varian SpectrAA 300 operating at wavelengths of 242.5 and 307.6 nm for cobalt and zinc, respectively. Because of the higher cobalt fraction x_{Co} experimentally determined by AAS compared to the cobalt amount used in synthesis (cf. Table 1), we conclude that the incorporation of cobalt is favored over zinc.

Notably, the reported synthesis procedure[17] for microcrystalline material of **1** proved to be successful only for the incorporation of small percentages of cobalt, as shown in EPR studies.[17] Nevertheless, by changing the reported method by the use of DMF instead of

dx.doi.org/10.1021/ic302643w | Inorg. Chem. 2013, 52, 4431−4442

Table 1. Comparison of x_{Co} Used in Synthesis with That Determined by AAS

	AAS	AAS
synthesis	Series I	Series II
0.00	0.00	0.00
0.02		0.03
0.05	0.09	0.06
0.10	0.17	0.13
0.20	0.25	
0.25	0.29	0.47
0.30	0.38	
0.50	0.75	0.58
0.75	0.99	0.99
1.00	1.00	1.00

ethanol, higher amounts of Co^{2+} could be incorporated in yields ranging from 40% to 98%, depending on composition.

X-ray Crystallography. The X-ray diffraction (XRD) data were collected on an IPDS-I (STOE) diffractometer using Mo−Kα radiation (λ = 71.073 pm).[41] The structure was solved by direct methods and refined using SHELX-97.[42] The coordinates of the framework non-hydrogen atoms were refined using anisotropic displacement parameters, whereas the disordered water molecules were treated isotropically. The coordinates of hydrogen atoms of the framework were calculated for idealized positions.

The PXRD (powder XRD) and TD-PXRD (temperature-dependent powder XRD) measurements were carried out on a STOE STADI-P diffractometer in Debye−Scherrer mode using Cu−Kα_1 radiation (λ = 154.060 pm). The samples for these measurements were prepared in glass capillaries (outer diameter, 0.5 mm). The TD-PXRD measurements were carried out in steps of 5 °C from room temperature up to 500 °C. Thermogravimetry measurements were performed on a Netzsch F1 Jupiter thermobalance.

Solid-State NMR. Solid-state NMR measurements were carried out at two different magnetic fields, 17.6 and 2.35 T. Experiments were performed at room temperature using 2.5, 4, and 7 mm MAS probes.

^{13}C Measurements. High-field experiments were done on a Bruker Avance 750 spectrometer operating at a field of 17.6 T and a ^{13}C resonance frequency of 188.41 MHz. To avoid overlap of spinning sidebands, ^{13}C CPMAS[43] spectra were acquired together with the TOSS (TOtal Sideband Suppression) sequence.[44] The spinning frequency was 10 kHz, and contact times of 100 μs and 1 ms were used to differentiate protonated and nonprotonated carbon signals. For cross-polarization, a ramped pulse[45] on the ^1H channel was employed; 300 and 360 scans were acquired for the protonated ligands **L1**$^-$ and **L2**$^-$ with recycle delays of 50 and 70 s, respectively. For the MOF samples **1** and **2**, 4000 and 1600 scans were collected with recycle delays of 5 and 10 s, respectively. The decoupling and Hartmann-Hahn matching fields were 80 and 65 kHz, respectively. The presence of paramagnetic Co^{2+} lowers the resolution of carbon spectra severely. Hence, only spectra for samples containing cobalt in low concentrations (up to 25%) were recorded. The corresponding spectra were recorded with recycle delays of 4 s or less, collecting 4000 scans.

Spectral editing experiments using nonquaternary suppression (NQS),[46] with two dephasing delays of 37 μs each within an echo sequence spanning two rotor periods helped in assignment. All measurements were done with high-power ^1H decoupling using two pulse phase modulation (TPPM).[47]

The 2D FSLG-HETCOR[29] experiments of the protonated ligand **L1**$^-$ and MOFs **1** and **2** were done at 10 and 8 kHz MAS and a contact time of 500 μs with 13 μs as the length of one FSLG block. For **L1**$^-$ and **1**, 80 and 128 t_1 increments were collected with 256 scans and 5 s as the recycle delay. For **2**, a recycle delay of 4 s and 400 transients with 128 t_1 increments were used. The States-TPPI[48] mode for pure absorption spectra was employed.

Chemical shifts are referenced to TMS using adamantane as a secondary reference with the downfield signal at 38.56 ppm.

^1H Measurements. High-field measurements at 17.6 T were done at a frequency of 749.32 MHz. Single pulse excitation experiments were performed at various spinning frequencies of 10, 11, 12, 12.5, and 25 kHz, in particular for high resolution and to distinguish signals from spinning sidebands. (π/2) pulse lengths were about 3.6 μs at 12.5 kHz and 1.4 μs at 25 kHz MAS. For the paramagnetic samples, since the uniform excitation of the full spectrum is hard to achieve with a single pulse, a frequency-stepped acquisition was performed. Therefore, for both static and MAS experiments (10 kHz spinning frequency), Hahn-echo[49] spectra with a 90° pulse length of 3.2 μs were measured at two different excitation frequencies of 104 and −104 kHz from the center of the main resonance and the full spectrum was obtained by summing up the individual subspectra.

2D $^1H-^1H$ BABA[30] double quantum experiments were performed using a 2.5 mm probe at a spinning frequency of 30 and 26 kHz for **1** and **2**, respectively; 128 points were collected in the indirect dimension with 16 and 64 scans and recycle delays of 1 and 3 s for **1** and **2**, respectively. During excitation and reconversion, the back-to-back (BABA) scheme was used, which recouples the $^1H-^1H$ dipolar coupling. (π/2) pulses were 1.6 μs, and recoupling over one rotor period was used. The *z*-filter delay was 20 μs. For pure-absorption spectra, the TPPI scheme was used.[50]

Static ^1H T_1 relaxation measurements were performed at a magnetic field of 2.35 T and a frequency of 100.13 MHz using a Tecmag Apollo spectrometer. The inversion recovery sequence[51] with (π/2) pulse lengths of 2.0 and 2.75 μs for **1** and **2**, respectively, was used. The sequence was combined with DEPTH[52] detection to remove probe background signal. The samples were packed in a 7 mm MAS rotor used under nonspinning conditions. The lower magnetic field was chosen for the relaxation measurements since, in this case, uniform excitation was possible.

All ^1H spectra were referenced to TMS using a sample of PDMS as secondary reference (0.07 ppm from TMS).

First-Principles NMR Calculations. Geometry optimizations and chemical shift calculations were carried out within the density functional theory (DFT) framework using the CASTEP (Cambridge Serial Total Energy Package) software.[32] CASTEP uses plane-wave basis sets to describe the wave functions (it thus has an implicit translational symmetry) and is very well adapted to the description of solid crystalline systems. The GIPAW (gauge-including projector augmented waves) method,[31] used with ultrasoft pseudo-potentials,[53,54] provides an efficient method for calculating chemical shifts in crystalline solids.[55] The geometry optimization of the X-ray determined structure and the calculation of NMR parameters were carried out using generalized gradient approximation (GGA) with the PBE exchange correlation functional[56] and Vanderbilt-type pseudo-potentials.[54] Only the proton positions were relaxed during the geometry optimization, keeping both the unit cell and all the other atoms fixed to their X-ray determined positions. For the geometry optimization, a plane-wave cutoff energy of 800 eV and a Monkhorst−Pack grid of *k*-points[57] spacing of 0.05 Å^{-1} in reciprocal space were used. The NMR calculations were done on the proton-optimized structure using a higher cutoff energy of 1000 eV and a *k*-point sampling of 0.05 Å^{-1}. The NMR converges slowly because the part of the electronic structure on which it depends converges slowly, therefore, a higher cutoff energy was used for the NMR calculations. To compare directly with experimentally measured isotropic chemical shifts, the calculated chemical shieldings were then converted into calculated chemical shifts, δ_{calc}, using the relation, $\delta_{calc} = \sigma_{ref} - \sigma_{calc}$. The value of σ_{ref} was determined with a linear regression between calculated and experimental shifts, imposing a slope of unity, where shifts and shielding were simply sorted by ascending and descending order, respectively. This procedure leads to a ^{13}C reference value of 169.65 ppm, which was then used to determine the computed chemical shifts.

dx.doi.org/10.1021/ic302643w | Inorg. Chem. 2013, 52, 4431−4442

RESULTS AND DISCUSSION

X-ray Diffraction Studies. Whereas the isomorphous Zn (**1**) and Zn/Co MOFs of Series I crystallize in the noncentrosymmetric monoclinic space group *Pc* (No. 7) with two formula units per unit cell, the coordination polymer **2** crystallizes in the noncentrosymmetric orthorhombic space group $Pca2_1$ (No. 29) with four formula units per unit cell. The atomic coordinates of **1** can be found in ref 17; those of **2** are reported in Table S 3 (Supporting Information). The formula units correspond to the asymmetric units in the crystal structures and consist of one metal ion, Zn^{2+} or Co^{2+}, and two ligand anions $(Me\text{-}3py\text{-}trz\text{-}pba)^-$ or $(Me_2trz\text{-}pba)^-$, respectively. In addition, the asymmetric unit of **2** contains 1.5 noncoordinated water molecules and one DMF molecule. The Zn^{2+} ions in **1** and **2** possess coordination spheres in the transition from trigonal-bipyramidal to square-pyramidal (see Figure 1). Selected bond lengths and angles of **1** and **2** are

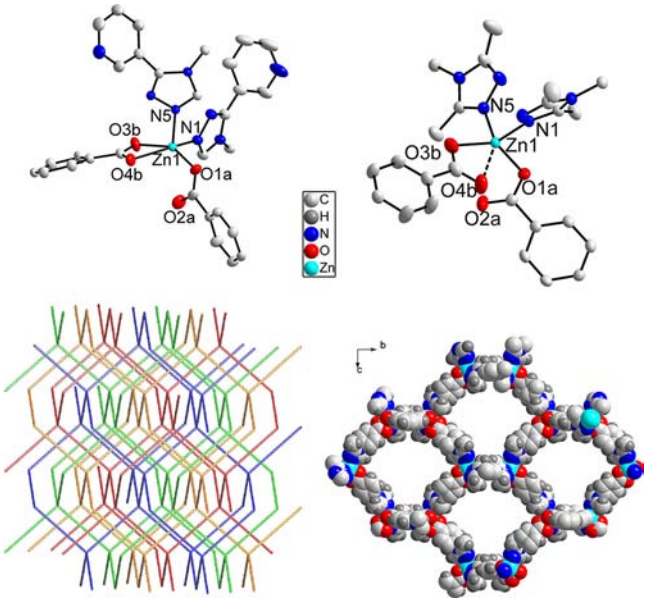

Figure 1. Top: Structural motif of coordination polymers **1** (left) and **2** (right). The atom labels for **2** correspond to the crystallographic data (CCDC 852802) and that of **1** published elsewhere.[17] Bottom: The four-fold interpenetrating networks of **1** (left) and 3D projection of a single net of **2** (right).

given in Table S 2 (Supporting Information). The topology of both series is the one of the commonly observed diamondoid network (**dia**, point symbol $\{6^6\}$), which was determined using the program TOPOS 4.0.[58] The porosity of these compounds is reduced by four-fold interpenetration (type Ia).[59]

The phase purity of the as-synthesized materials was proven by powder X-ray diffraction. The powder patterns are in good agreement with the respective simulated patterns for both **1** and **2**, as shown in Figure 2. Additionally, all mixed zinc/cobalt MOFs were obtained as phase pure materials; no byproducts are observed, showing that there is no miscibility gap in both series. The crystallographic data were deposited as CCDC codes 783568, 783569, and 852802.

Solid-State NMR. *^{13}C NMR.* Figure 3 compares the ^{13}C CPMAS spectra of the Zn MOFs **1** and **2** and the corresponding protonated ligands. Four distinct functional regions ascribed to methyl, aromatic, pyridine-triazole, and carboxyl carbons are well separated in the ranges of 10−13, 120−140, 144−160 ppm, and above 165 ppm, respectively.

Several differences are visible when comparing the NMR spectra of the same ligands incorporated into the 3D MOF network. It is noteworthy to point out the reduced line widths of the signals in the MOF spectra in comparison to its uncoordinated ligand, which indicates a higher degree of order in the coordination framework.

A doubling of MOF resonances with respect to the protonated ligand is clearly evident from the ^{13}C CPMAS spectra (see Figure 3). As reported before,[60,61] this is due to the different relative orientation of the two ligands in the asymmetric unit of the respective crystal structures. For example, in the coordination polymer **1**, the carboxyl group of the ligand $\mathbf{L1}^-$ is coordinated to the Zn^{2+} ion in a monodentate, in the second ligand, in a bidentate mode. The torsion angle between phenyl-triazole and triazole-pyridine rings are found to be 90° and 40° for the monodentate binding ligand, respectively. However, these values change to 78° and 56°, for the bidentate binding ligand. This leads to different electronic environments and thus results in different chemical shifts, leading to two signals for each carboxyl carbon atom. This is also in agreement with the results from the NMR-CASTEP calculations (see below) and can be documented by the different carbon−oxygen distances for the same carbon atom in the two nonequivalent ligand molecules.

Since the ligand $\mathbf{L2}^-$ is symmetric about the C_2 axis, the corresponding MOF spectrum possesses a more simple signal pattern additionally to the fact that the pyridine ring is absent. Metal binding via one nitrogen of the triazole ring and carboxyl oxygens (both mono- and bidentate) induces asymmetry, leading to a doubling of resonances as for **1**. However, smaller chemical shift differences between the same carbon atoms in two nonequivalent ligand molecules are obtained due to the higher symmetry, and therefore, fewer signals than for **1** are resolved.

Some signals are significantly shifted in the spectrum of the MOF samples with respect to the protonated ligand, mainly due to metal coordination. This effect of metal coordination to the ligand molecule can be analyzed by calculating the coordination induced shifts,[60,62] obtained by subtracting from the carbon chemical shifts of the MOF those of the corresponding uncoordinated ligand. These numbers are summarized for the most significant carbon atoms in Table 2.

Table 2. ^{13}C NMR Coordination Induced Shifts, $\Delta\delta$ for 1 and 2

carbon	$\Delta\delta_1 = \delta_{MOF} - \delta_{lig}$	$\Delta\delta_2 = \delta_{MOF} - \delta_{lig}$
C-1	+5.7, +6.3	+3.2, +5.3
C-2	+2.0, −0.3	+0.0, +0.2
C-9	+4.9, +3.5	+3.3
C-10	+0.2, +1.6	+2.2

The carboxyl carbon (C-1) is found to be most sensitive to metal coordination[60,63,62] in both MOFs. While incorporated into **1**, this signal gets shifted downfield by 5.7 and 6.3 ppm, which clearly corroborates the metal binding via the carboxyl group; however, for **2**, the effects are somewhat smaller. The shift difference for C-1 also induces a shift effect on the neighboring carbon C-2 as well.

dx.doi.org/10.1021/ic302643w | Inorg. Chem. 2013, 52, 4431−4442

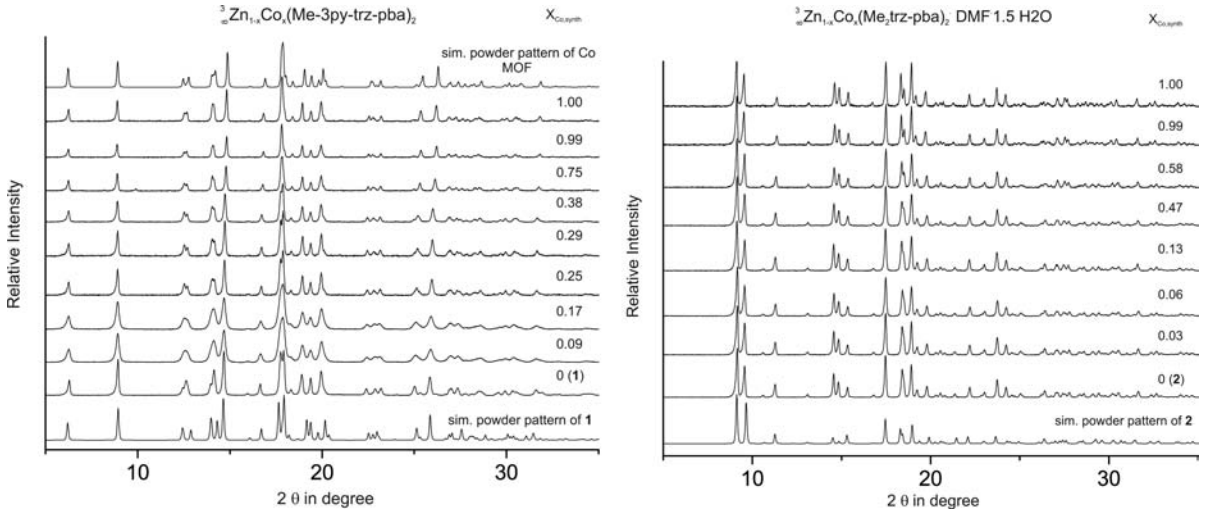

Figure 2. X-ray powder patterns of MOFs from Series I (left) and Series II (right) together with the simulated powder patterns for the pure Zn and pure Co compounds. For the pure Co MOF in Series II, no single crystal structure is available.

A large $\Delta\delta$ value has also been observed for carbon C-9 of the triazole ring, implying the effect of metal coordination through its nearby nitrogen atom. However, this value being smaller than that of C-1 predominantly refers to a relatively larger metal−carbon distance[64] (e.g., 263/250 pm for C-1 vs 309/313 pm for C-9 for **1**). In contrast to C-9, C-10 shows a smaller $\Delta\delta$ value, indicating a comparatively larger distance to the metal center (411 pm for **1**) and documenting binding via the nitrogen next to C-9. For **2**, the shift effects are less pronounced, though also showing the largest induced shifts for carbons C-1 and C-9.

Other carbons not involved in metal binding typically show small shift differences between protonated ligand and MOF, which could be explained by the different $\pi-\pi$ stacking interactions in the uncoordinated ligand and the interpenetrated frameworks.

The full resonance assignments given in the Supporting Information were achieved by a combination of several techniques. Spectral editing (NQS and different contact times, details given in the Supporting Information, Figures S 4−S 7) allowed us to distinguish protonated and quaternary carbons (as well as mobile, rotating groups, such as methyl groups). Comparison to literature values for similar compounds as well as the solution NMR data of structurally similar triazolyl ligands[16] helped in refinement.

For **1**, NMR-CASTEP calculation results are included in Figure 3 and in Table S 4 (Supporting Information), showing a very good agreement with the experimental spectrum. In accordance with the discussion of the crystal structure, two signals are present for every carbon atom of the ligand and results in a total of 30 lines. The deviation between experimental and calculated values might hint at a somewhat dynamic structure at room temperature.

The assignment based on the calculated values are further revealed by FSLG-HETCOR experiments, as shown in Figure 4 for **1** and **2** (for the protonated ligand $\mathbf{L1}^-$ shown in the Supporting Information, Figure S 8). The spreading of signals in two dimensions as well as the higher resolution in the indirect dimension from the homonuclear Lee−Goldburg decoupling enhances the information content.

Especially for **1**, resolution of different ^{1}H chemical shifts and the cross-peaks from the methyl protons to carbons C-9, C-5, and C-6 strengthen our assignments. For **2**, the presence of four signals (two of them overlapping) for the four methyl groups is clearly visible, and the respective protons of these methyl groups show a different coupling to the C-9 and C-10 carbon atoms. This means that the orientation in the crystal structure makes all methyl groups nonequivalent. A solvent signal at 162.2 ppm is identified by having unique coupling to a proton with no other cross-peaks. For ligand $\mathbf{L1}^-$, the resonance at 153.1 ppm could be clearly assigned to C-9 due to the cross-peak with the methyl protons (see the Supporting Information, Figure S 8).

^{1}H NMR. The metal coordination by the oxygen atoms of the carboxylic group is clearly documented from the ^{1}H MAS spectra (shown in the Supporting Information, Figure S 9) by the disappearance of the carboxylic acid proton at chemical shifts of 15.0 and 16.5 ppm for **1** and **2**, respectively. For **2**, two regions of signals around 7.5 ppm for aromatic and 2.0 ppm for methyl protons are visible. For **1**, however, the methyl signal is more narrow than in the corresponding protonated ligand and shifted 1 ppm downfield. Furthermore, aromatic signals span a range from 5 ppm up to 9 ppm. This larger range compared to that of **2** is due to the additional pyridine ring in the ligand.

To get more information from the ^{1}H spectra, we combine the information from the MAS spectrum with the results from the NMR-CASTEP calculations (for **1**, experimental and calculated values are given in the Supporting Information, Table S 5) and the ^{1}H projection from the FSLG-HETCOR spectrum with higher resolution (see above). Furthermore, the 2D ^{1}H−^{1}H double quantum BABA spectrum gives further insight from ^{1}H−^{1}H correlations, as shown in Figure 5, for **1** and **2** together with the MAS spectrum, the calculated spectrum, and the FSLG-HETCOR projection. In the HETCOR projection, the resolution is higher due to the homonuclear decoupling. In the 2D BABA spectrum, diagonal peaks indicate the proximity of two protons with the same chemical shifts. Off-diagonal peaks then identify the proximity of two protons with different chemical shifts, the corresponding shift in the double-quantum dimension being the sum of the chemical shifts of the two involved protons.

As seen in Figure 5, there is a very good agreement between experimental and calculated chemical shifts. Differences are seen predominantly only for the signals at 4.2 and 4.4 ppm in

dx.doi.org/10.1021/ic302643w | *Inorg. Chem.* 2013, 52, 4431−4442

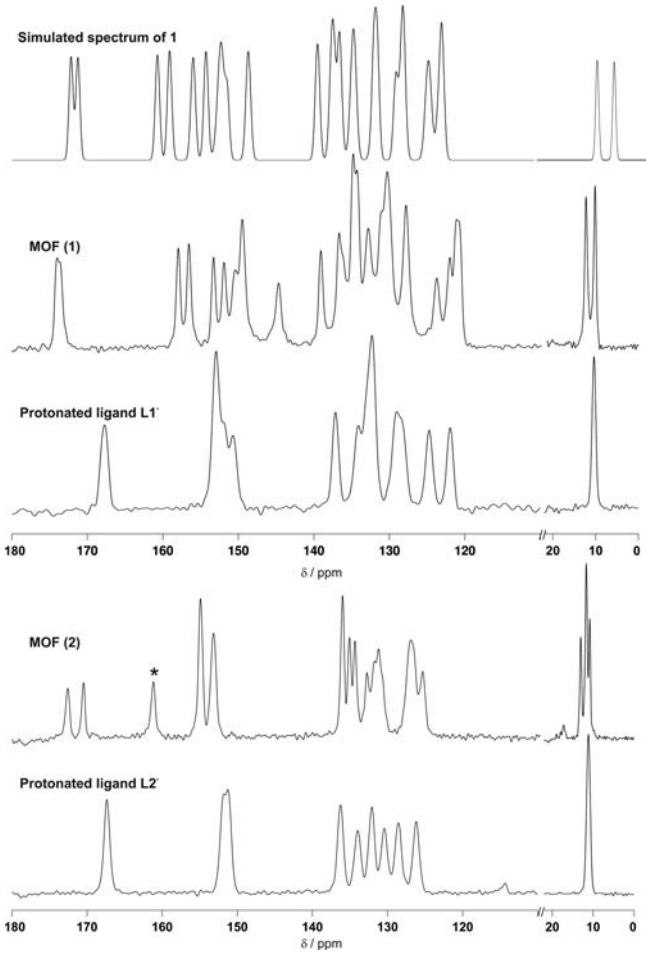

Figure 3. ^{13}C CPMAS spectra of **1** and **2** in comparison with their corresponding protonated ligands. The spectral range between 20 and 110 ppm with no signal intensity is cut out to enlarge the relevant signal areas. The asterisk indicates a solvent signal from DMF that resides in the pores. The remaining DMF peaks (30.1 and 35.2 ppm) are not shown since the axis break starts at 20 ppm. The spectrum of **1** simulated based on the results of the CASTEP calculations is also included for comparison (top), with all carbon signals having equal intensity and identical line width (for simplicity, the line width of the 150 ppm peak is used for simulation).

the calculated spectrum. Intensity differences between the different ^{1}H spectra arise from the different excitation efficiencies in the BABA and HETCOR spectra.

The assignments were made by combining the CASTEP results with the observed cross-peaks in the FSLG-HETCOR spectrum. The protons of the aromatic ring have rather typical chemical shifts with the exception of one of the H6 protons at 9.3 ppm, which agrees well with the calculated value. The protons of the pyridine ring, H13 and H14, are found at rather low chemical shifts, 4.9 and 5.2 ppm, respectively. These values presumably result from the shielding of these protons that are positioned above (below) the face of aromatic rings.[65]

The 2D BABA spectra show close through-space proximity of protons. Most clearly, this can be seen for **2**. Because of the small shift range of both aromatic and methyl signals, no resolution of coupling within the aromatic or the methyl region is possible. However, off-diagonal peaks between aromatic and methyl signals are visible. These arise between the methyl protons and the protons at the C-4 and C-6 carbons. For compound **1**, several correlation peaks are resolved because of the larger shift range within the aromatic range between 9.3 ppm for H6 and 4.9 ppm for H13 (see above). On the basis of the assignment of proton signals from the CASTEP calculations and the FSLG-HETCOR spectrum, all expected correlation signals can be found. Especially, at least three correlation peaks between the aromatic and methyl region can be identified, corresponding to the protons H4 and H6 from the aromatic ring (compare Scheme 1 for through-space distances). H12 shows no correlation peak, as expected. This can be seen, however, only at lower magnification of the 2D plot (not shown). Because of short excitation and reconversion times, intermolecular cross-peaks between the interpenetrated networks are not observed in the 2D BABA experiment. The results show that 2D BABA experiments can be well used to identify the proton shifts by their coupling scheme.

HETERONUCLEAR MOFS

The presence of traces of paramagnetic impurities in the sample has various effects on NMR spectra, such as unusual chemical shifts, dramatic line broadening, and shortening of relaxation times. The hyperfine interaction[66] is responsible for the unusual chemical or paramagnetic shifts, the size of which is often hard to predict and can lead to shifts of up to 1000 ppm for ^{13}C.

Since magic-angle spinning removes only the isotropic part of the magnetic susceptibility, contributions from the anisotropic bulk magnetic susceptibility and short T_2 also lead to the broadening of resonances. The demagnetizing fields created, for example, at grain boundaries, influence neighboring spins, and hence these orientation-dependent local fields cause a dispersion of chemical shifts and result in broadening of NMR resonances. This phenomenon has been investigated in the pioneering works by Lippmaa and VanderHart.[67,68] Additionally, the presence of large magnetic susceptibilities in the sample even produces a large manifold of spinning sidebands in MAS spectra,[69,70] which can be analyzed in a similar way as chemical shift anisotropy.

The combined effects of hyperfine interaction and anisotropic magnetic susceptibility limit good spectral resolution in our samples, both for ^{1}H and ^{13}C spectra (see discussion below). Nevertheless, NMR relaxation measurements can be used to analyze the dynamics and distribution of paramagnetic centers in the matrix of diamagnetic ions.[71,72] It is noteworthy to point out the improvements in the detection and resolution of ^{1}H and ^{13}C signals in paramagnetic systems using fast magic-angle spinning by Ishii et al.[73−75]

Effect of Paramagnetic Co^{2+} on the ^{13}C and ^{1}H NMR Spectra. For the demonstration of the influence of paramagnetic Co^{2+} on the NMR measurements, both ^{13}C and ^{1}H spectra were recorded. Figure 6 exemplifies the ^{13}C spectra of MOFs from Series I with Co^{2+} amounts of $x = 0.09$ and 0.17 in comparison to the pure zinc compound **1** (see Figure S 10, Supporting Information, for Series II).

In contrast to the diamagnetic MOF **1**, the corresponding paramagnetic analogues have a rather low resolution due to broadening by the paramagnetic cobalt ions, with the isotropic shifts being unchanged. Different efficient decoupling sequences[76,77] were applied to improve resolution, but they showed no improvement. Also, higher spinning frequencies (>25 kHz) with or without decoupling did show no improvement, as, for instance, observed for copper-containing samples.[73] In our cobalt-containing samples, the couplings are probably much stronger due to the higher number of unpaired electrons. Contrary to reports on NMR of paramagnetic systems,[78] here

dx.doi.org/10.1021/ic302643w | Inorg. Chem. 2013, 52, 4431−4442

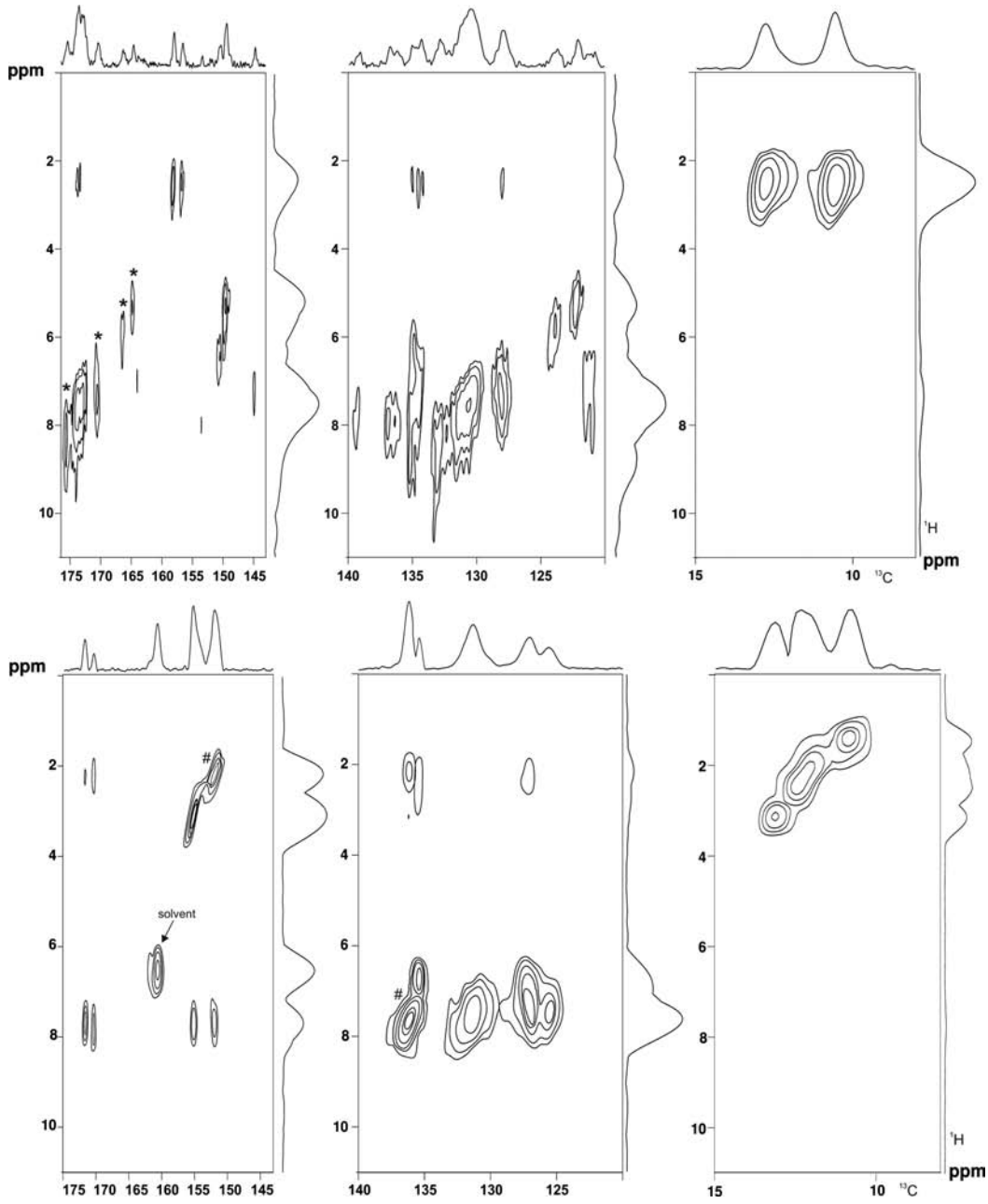

Figure 4. 2D ^{1}H−^{13}C FSLG HETCOR spectra of **1** (top) and **2** (bottom). Individual ^{1}H projections for the different ^{13}C regions are shown. The asterisks indicate spinning sidebands. Coherences marked with a # indicate the resolution of carbon signals in the 2D plot that are not resolved in the ^{13}C CPMAS spectrum, as can be seen by the nonspherical shape of the coherences.

by no means any additional carbon shifts were detected, but only severe line broadening is observed. Our current explanation is that we cannot detect those ^{13}C spins in direct vicinity of Co^{2+}, which either might have shifted to some totally unpredictable range or more probably are severely broadened to be indistinguishable from the baseline.[79] The line broadening of the remaining ^{13}C spins next to Zn^{2+} then indicates reduction in T_2 or T_2^* due to the presence of nearby cobalt ions, thus indicating the formation of a heteronuclear Co/Zn MOF.

Figure 7 illustrates the line-broadening effects for various regions of carbon signals with increasing cobalt content. Note that, for the diamagnetic spectra, a line broadening of 5 Hz has been applied. It can be seen that the line broadening increases almost exponentially with the cobalt content, and for $x \geq 0.25$, no reasonable spectra can be obtained. Regarding functional groups, the increase in line width is comparatively small for the regions of 8−16, 155−160, and 170−176 ppm (range I) compared to the regions of 120−141 and 143−155 ppm (range II). To quantify it more precisely, we calculated the corresponding slopes by omitting the value at x_{Co} = 0.25 by a linear fit. The slopes are found to be almost the same in range I, being 40% smaller than those in range II. This lets us conclude that the line broadening is strongly influenced by the bulk magnetic susceptibility[68] originating from the paramagnetic ions, which shows no preference to functional groups. The broadening effect is enhanced in condensed aromatic systems, which probably can be explained by stronger electron−electron interactions between the cobalt electrons and the π-electron systems of the aromatic and triazole rings.

dx.doi.org/10.1021/ic302643w | *Inorg. Chem.* 2013, 52, 4431−4442

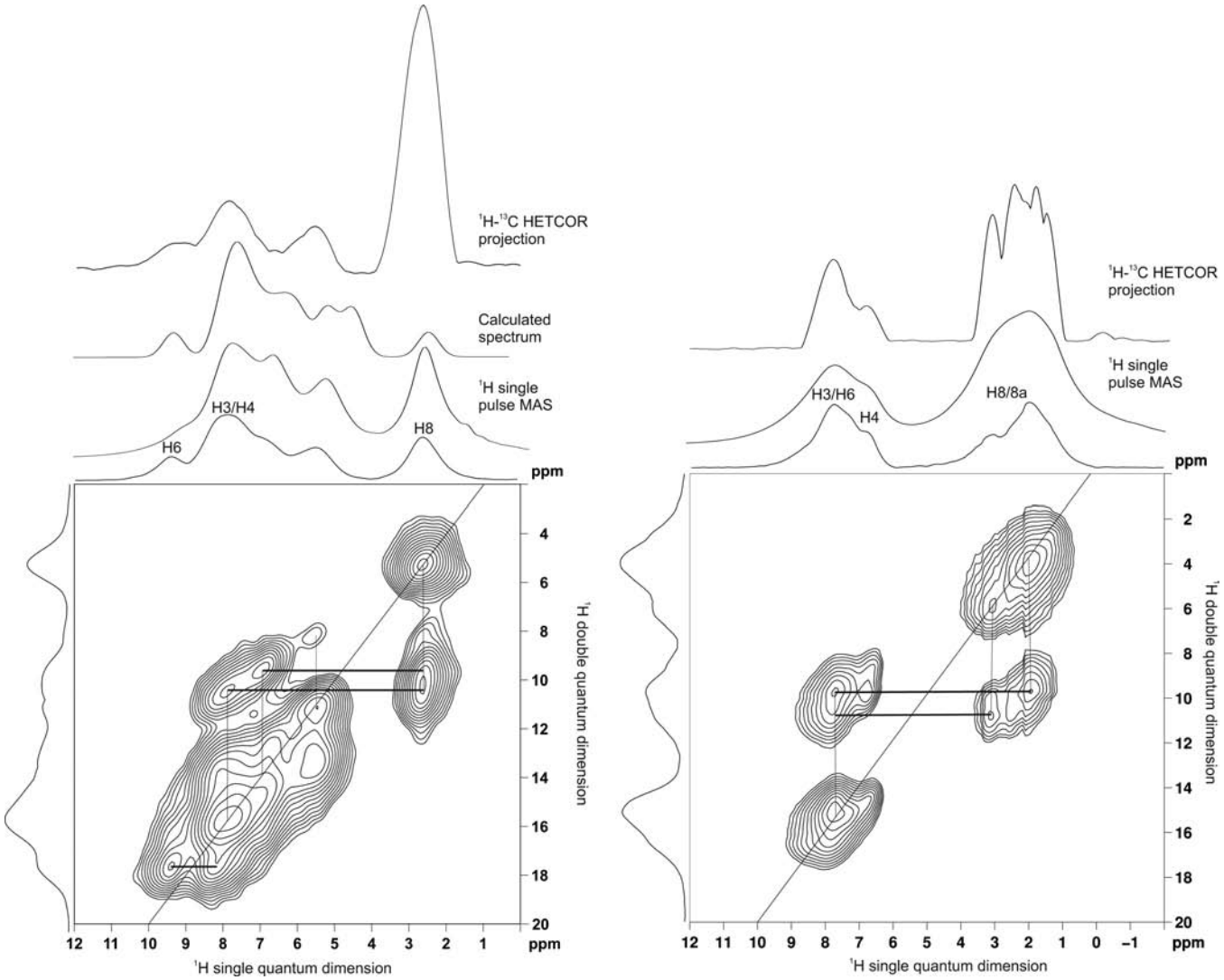

Figure 5. 2D ^{1}H BABA spectrum of **1** (left) and **2** (right) recorded at a spinning frequency of 30 and 26 kHz, respectively. The ^{1}H single pulse MAS spectrum, the calculated spectrum based on the CASTEP results (for **1**), and the ^{1}H projection of the ^{1}H−^{13}C HETCOR spectrum are also shown for comparison. The horizontal lines in the 2D spectrum indicate selected correlations between coupled protons, H8−H3/H4, H8−H6, H6−H4 (left) and H8/8a−H4, H8/8a−H3/H6 (right).

^{1}H 1D spectra and ^{1}H T_1 relaxation experiments can also be used to monitor the influence of paramagnetic Co^{2+} in the MOF lattice. ^{1}H MAS and static spectra for all samples were collected at 17.6 T, as illustrated for the MAS spectra of Series I in Figure 8. Without cobalt, the spectrum shows individual resonances, followed by a narrow sideband pattern due to homonuclear ^{1}H−^{1}H dipolar coupling. However, with increasing cobalt content in the isotropic region, only one signal can be resolved. Additionally, a wide sideband pattern extending up to 490 kHz is visible as a result of the inhomogeneous electron−nucleus dipolar interaction.[69]

The ^{1}H static linewidths (fwhh = full width at half-height) recorded at two magnetic fields are shown as a function of cobalt content in Figure 9. A steady increase in line width with increasing cobalt content is observed, with the effect being larger at higher field. This observation is supported by the literature,[67] where it has been shown that the major contribution to the line broadening comes from the electron−nuclear interaction, which has been shown to be linear dependent on magnetic field. We note that, for sample x_{Co} = 0.09 and 0.17 for Series I at 17.6 T, the ^{1}H line width is slightly smaller than that at 2.35 T. We assign this to experimental uncertainties that do not contradict the general observation.

Influence of Co^{2+} on the ^{1}H Spin−Lattice Relaxation Time. The influence of paramagnetic ions on the proton relaxation times has been studied by several authors.[80−82] It is the fluctuating electron magnetic moments of paramagnetic centers that affect the nuclear relaxation. Protons in the immediate vicinity of Co^{2+} ions (high-spin) are directly influenced. In fact, their longitudinal relaxation time gets severely shortened, and we assume that we cannot measure their short spin−lattice relaxation time.[82] These protons act as relaxation sinks that influence the relaxation behavior of other distant protons via efficient spin diffusion. Therefore, the measured T_1^H is the average relaxation time of all the protons together.

There are two different possibilities for the distribution of Co^{2+} in the host framework: either it forms Co^{2+}-rich domains separated from Zn^{2+}-rich ones or both metal ions are distributed uniformly and only one domain can be identified. In the first case, two relaxation rates would be expected for Zn^{2+}

dx.doi.org/10.1021/ic302643w | Inorg. Chem. 2013, 52, 4431−4442

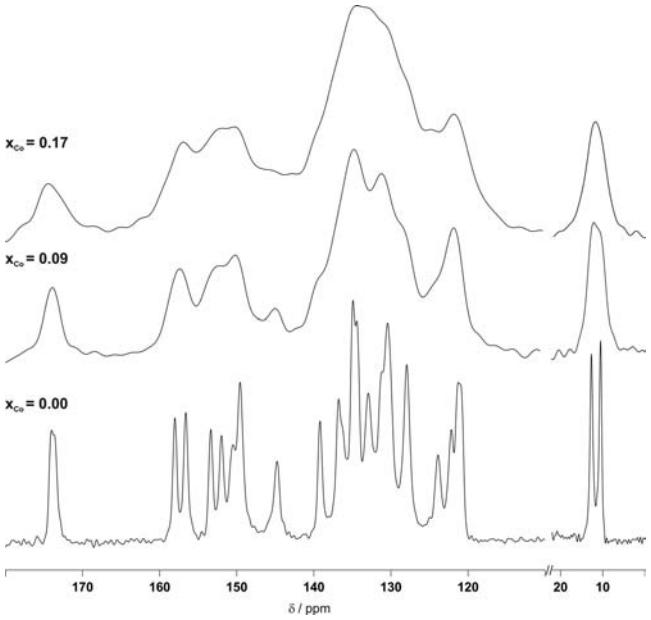

Figure 6. ^{13}C CPMAS spectra for selected samples of Series I, showing the influence of paramagnetic cobalt.

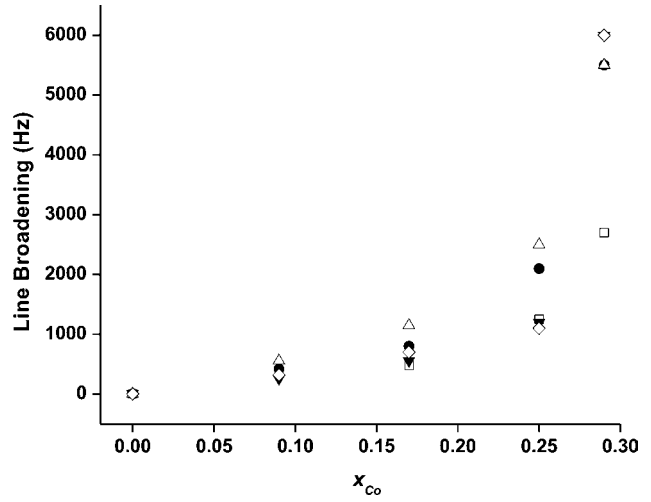

Figure 7. Line-broadening effect determined from application of exponential multiplication to the ^{13}C signal of the pure zinc compound **1** to match the experimental line width for the cobalt-containing samples of Series I as a function of Co concentration for individual signal regions. Notation of symbols: 8–16 (□), 120–141 (●), 143–155 (Δ), 155–160 (▼), and 170–176 ppm (◇).

and Co^{2+} domains separately, whereas in the second case, only one.

All the relaxation curves obtained could be well-fitted with a single exponential function. The relaxation times are found to be strongly influenced by the paramagnetic Co^{2+}, with a larger effect at higher cobalt concentration. The paramagnetic contribution to the proton T_1 can be calculated using the sum-of-rates equation[71] as

$$\frac{1}{T_1} = \frac{1}{T_1^{pure}} + \frac{1}{T_1^{para}} \quad (1)$$

where T_1^{para} represents the paramagnetic contribution to the relaxation and T_1^{pure} is the ^{1}H T_1 relaxation time of the pure Zn MOF. The $1/T_1^{para}$ values as a function of Co^{2+} content for the

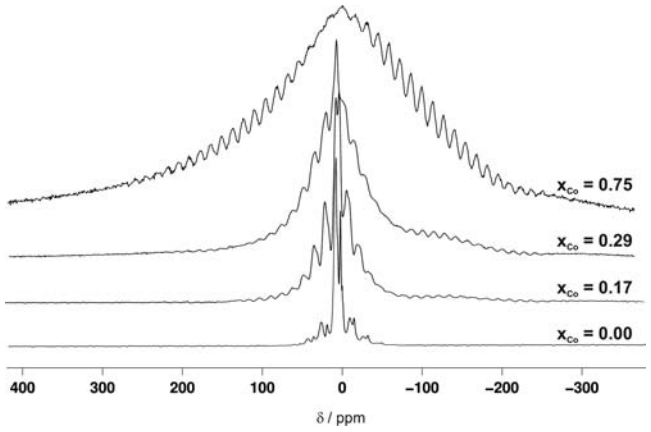

Figure 8. ^{1}H MAS spectra recorded at 17.6 T for selected samples of Series I.

two series at 2.35 T are shown in Figure 10 (left). For both series, the strong influence of paramagnetic cobalt on $1/T_1^{para}$ is clearly documented from the linear relation.

Figure 10 (right) shows a correlation between the minimum cobalt–cobalt distance and $1/T_1^{para}$. The former is calculated from the known metal–metal distances from the crystal structure and the relative content of cobalt. This indicates a uniform distribution of cobalt within the MOF framework because the average distance between cobalt centers as a source of relaxation decreases with increasing cobalt content. For cobalt contents higher than 50%, the minimum cobalt–cobalt distance is constant since the first two metal neighbors have equal distance in the crystal structure. Clearly, the presence of more cobalt atoms influences the ^{1}H relaxation even further but cannot be expressed from the minimum cobalt–cobalt distance. However, the analysis of ^{1}H spin–lattice relaxation times indicates that, for the whole range of cobalt concentrations, a uniform distribution of zinc and cobalt metal centers is present.

CONCLUSIONS

The crystal structures of two series of isomorphous MOFs have been determined. ^{1}H and ^{13}C chemical shifts of both series of Zn MOFs are reported and compared to their corresponding protonated ligands. The effect of metal coordination is monitored by changes in the chemical shifts of those carbon atoms participating in the metal coordination, which is as large as 6.3 ppm. ^{13}C assignments were achieved by combining the different methods, spectral editing, heteronuclear correlation spectra, and CASTEP calculations for **1**. The two ligand molecules in the asymmetric unit give rise to one signal set each that is clearly documented in the ^{13}C spectra.

The assignments of ^{1}H chemical shifts was done based on the ^{1}H projections from the FSLG-HETCOR experiments and CASTEP calculations for **1**. These were verified by the 2D double quantum BABA spectra that identify close couplings between different protons. Rather high (9.3 ppm) and low (5.0 ppm) shifts for aromatic protons are observed that agree with calculations and the latter can be explained, for example, by the shielding of these protons which are positioned above (below) the face of the aromatic rings.

In two series of heteronuclear MOFs, the incorporation of paramagnetic Co^{2+} into the MOF structure being able to replace the Zn^{2+} ion in the full range of concentrations is documented by an increased line width in the ^{1}H and ^{13}C NMR spectra. Furthermore, a correlation of the paramagnetic

dx.doi.org/10.1021/ic302643w | Inorg. Chem. 2013, 52, 4431–4442

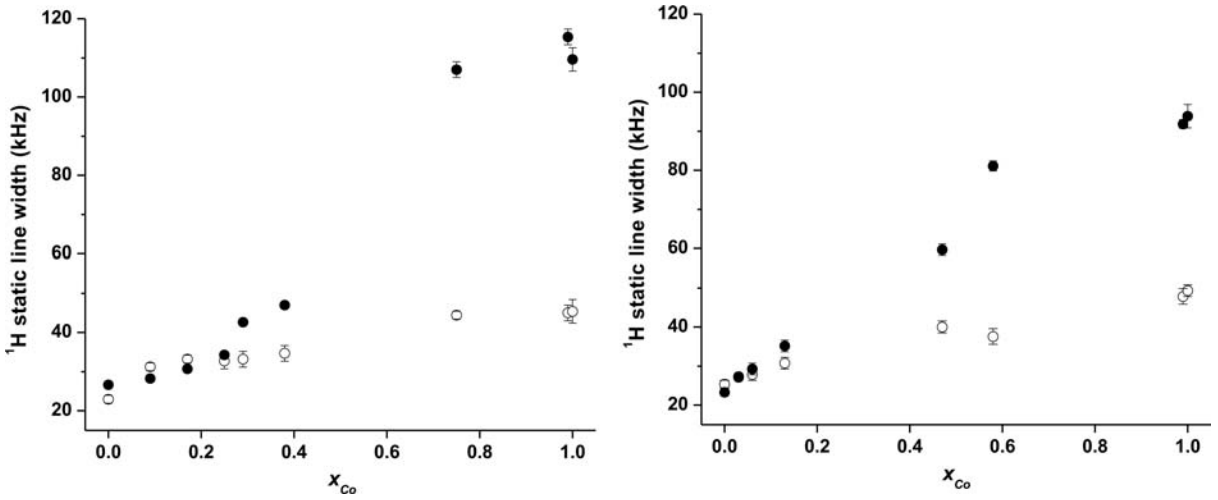

Figure 9. ^{1}H static line width of Series I (left) and Series II (right) as a function of cobalt concentration recorded at magnetic fields of 2.35 T (open circles) and 17.6 T (solid circles).

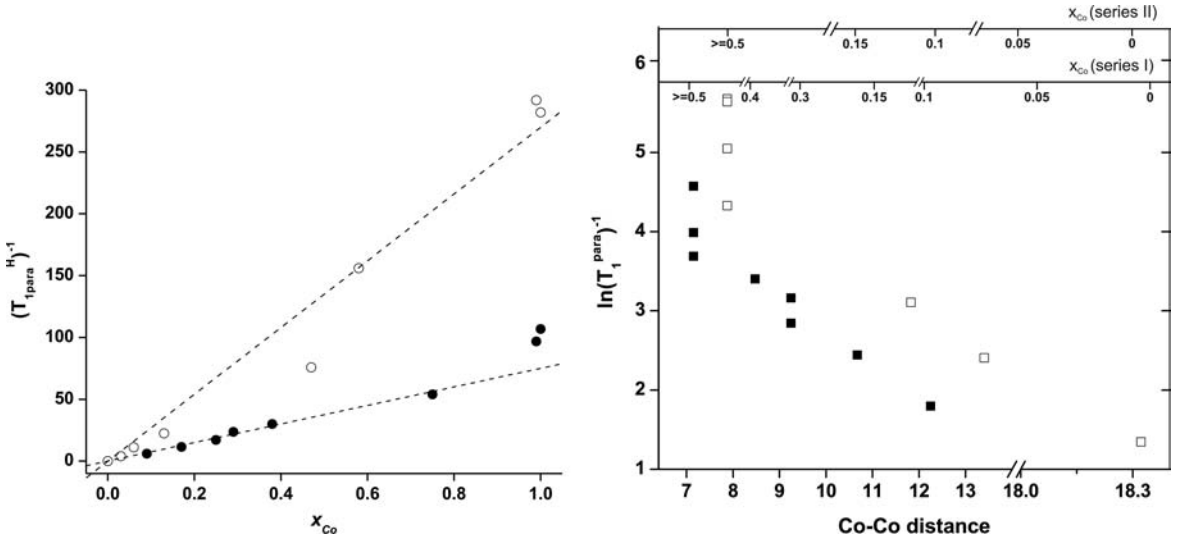

Figure 10. Left: Paramagnetic contribution to the ^{1}H spin−lattice relaxation as a function of cobalt content measured at a magnetic field of 2.35 T for Series I (solid circles) and Series II (open circles). Right: Correlation of minimum Co−Co distance with paramagnetic contribution to the ^{1}H spin−lattice relaxation for Series I (solid squares) and Series II (open squares). At the top of the diagram, the relation between Co−Co distance and cobalt content for both series of MOFs is illustrated.

contribution to the ^{1}H spin−lattice relaxation time with the minimum Co−Co distance was obtained, which corroborates a uniform distribution of Co^{2+} and Zn^{2+} in the MOF structure.

With this contribution, we have documented that the combination of different solid-state NMR techniques shows excellent agreement with predictions of chemical shifts based on X-ray structures and DFT calculations. Though this probably has to be verified on other MOF materials, we expect that, in the future, solid-state NMR can be used as a standard technique for the characterization of MOFs, especially for those with low crystallinity or even those lacking crystallinity. These materials might still show excellent properties for different applications. We will orient our efforts in this direction.

■ ASSOCIATED CONTENT

Ⓢ Supporting Information

IR, thermogravimetric, and temperature-dependent PXRD data and atomic coordinates of **2** are given in the Supporting Information. It also contains various CP spectra using spectral editing techniques; tables for ^{13}C and ^{1}H assignments; and additional ^{1}H 1D, ^{13}C CPMAS, 2D HETCOR, and BABA spectra. This material is available free of charge via the Internet at http://pubs.acs.org. CCDC 852802 contains the supplementary crystallographic data for this paper. These data can be obtained free of charge from The Cambridge Crystallographic Data Centre via www.ccdc.cam.ac.uk/data_request/cif.

■ AUTHOR INFORMATION

Corresponding Author

*E-mail: bertmer@physik.uni-leipzig.de.

Notes

The authors declare no competing financial interest.

■ ACKNOWLEDGMENTS

We thank the DFG (German Research Foundation) and the Experimental Physics Institute of Leipzig University for support with the Avance 750 MHz NMR spectrometer. A.V.K. thanks

the graduate school BuildMoNa for a doctoral stipend. D.L. acknowledges the fellowship of the Fonds der Chemischen Industrie, and J.L. acknowledges the ESF fellowship.

REFERENCES

(1) James, S. L. *Chem. Soc. Rev.* **2003**, *32*, 276−288.
(2) Kitagawa, S.; Kitaura, R.; Noro, S.-i. *Angew. Chem., Int. Ed.* **2004**, *43*, 2334−2375.
(3) Janiak, C.; Vieth, J. K. *New J. Chem.* **2010**, *34*, 2366−2388.
(4) Janiak, C. *Dalton Trans.* **2003**, 2781−2804.
(5) Li, H.; Eddaoudi, M.; O'Keeffe, M.; Yaghi, O. M. *Nature* **1999**, *402*, 276−279.
(6) Rosi, N. L.; Eckert, J.; Eddaoudi, M.; Vodak, D. T.; Kim, J.; O'Keeffe, M.; Yaghi, O. M. *Science* **2003**, *300*, 1127−1129.
(7) Lee, J.; Farha, O. K.; Roberts, J.; Scheidt, K. A.; Nguyen, S. T.; Hupp, J. T. *Chem. Soc. Rev.* **2009**, *38*, 1450−1459.
(8) Achmann, S.; Hagen, G.; Kita, J.; Malkowsky, I.; Kiener, C.; Moos, R. *Sensors* **2009**, *9*, 1574−1589.
(9) Lee, J. Y. Y.; Olson, D. H.; Pan, L.; Emge, T. J.; Li, J. *Adv. Funct. Mater.* **2007**, *17*, 1255−1262.
(10) Jeremias, F.; Khutia, A.; Henninger, S. K.; Janiak, C. *J. Mater. Chem.* **2012**, *22*, 10148−10151.
(11) Henninger, S. K.; Jeremias, F.; Kummer, H.; Janiak, C. *Eur. J. Inorg. Chem.* **2012**, *2012*, 2625−2634.
(12) Ehrenmann, J.; Henninger, S. K.; Janiak, C. *Eur. J. Inorg. Chem.* **2011**, *2011*, 471−474.
(13) Henninger, S. K.; Habib, H. A.; Janiak, C. *J. Am. Chem. Soc.* **2009**, *131*, 2776−2777.
(14) Jaap G, H. *Coord. Chem. Rev.* **2000**, *200−202*, 131−185.
(15) Zou, R.-Q.; Cai, L.-Z.; Guo, G.-C. *J. Mol. Struct.* **2005**, *737*, 125−129.
(16) Lässig, D.; Lincke, J.; Krautscheid, H. *Tetrahedron Lett.* **2010**, *51*, 653−656.
(17) Lässig, D.; Lincke, J.; Griebel, J.; Kirmse, R.; Krautscheid, H. *Inorg. Chem.* **2010**, *50*, 213−219.
(18) Lincke, J.; Lässig, D.; Moellmer, J.; Reichenbach, C.; Puls, A.; Moeller, A.; Gläser, R.; Kalies, G.; Staudt, R.; Krautscheid, H. *Microporous Mesoporous Mater.* **2011**, *142*, 62−69.
(19) Tonigold, M.; Lu, Y.; Bredenkötter, B.; Rieger, B.; Bahnmüller, S.; Hitzbleck, J.; Langstein, G.; Volkmer, D. *Angew. Chem., Int. Ed.* **2009**, *48*, 7546−7550.
(20) Paluch, P.; Potrzebowski, M. J. *Solid State Nucl. Magn. Reson.* **2009**, *36*, 103−109.
(21) Jiang, Y.; Huang, J.; Kasumaj, B.; Jeschke, G.; Hunger, M.; Mallat, T.; Baiker, A. *J. Am. Chem. Soc.* **2009**, *131*, 2058−2059.
(22) Habib, H. A.; Hoffmann, A.; Hoppe, H. A.; Janiak, C. *Dalton Trans.* **2009**, 1742−1751.
(23) Gul-E-Noor, F.; Jee, B.; Pöppl, A.; Hartmann, M.; Himsl, D.; Bertmer, M. *Phys. Chem. Chem. Phys.* **2011**, *13*, 7783−7788.
(24) Habib, H. A.; Hoffmann, A.; Höppe, H. A.; Steinfeld, G.; Janiak, C. *Inorg. Chem.* **2009**, *48*, 2166−2180.
(25) Shustova, N. B.; Ong, T.-C.; Cozzolino, A. F.; Michaelis, V. K.; Griffin, R. G.; Dinca, M. *J. Am. Chem. Soc.* **2012**, *134*, 15061−15070.
(26) Vukotic, V. N.; Harris, K. J.; Zhu, K.; Schurko, R. W.; Loeb, S. J. *Nat. Chem.* **2012**, *4*, 456−460.
(27) Kong, X.; Scott, E.; Ding, W.; Mason, J. A.; Long, J. R.; Reimer, J. A. *J. Am. Chem. Soc.* **2012**, *134*, 14341−14344.
(28) Lincke, J.; Lässig, D.; Stein, K.; Moellmer, J.; Viswanath Kuttatheyil, A.; Reichenbach, C.; Moeller, A.; Staudt, R.; Kalies, G.; Bertmer, M.; Krautscheid, H. *Dalton Trans.* **2012**, *41*, 817−824.
(29) van Rossum, B. J.; Förster, H.; de Groot, H. J. M. *J. Magn. Reson.* **1997**, *124*, 516−519.
(30) Feike, M.; Demco, D. E.; Graf, R.; Gottwald, J.; Hafner, S.; Spiess, H. W. *J. Magn. Reson., Ser. A* **1996**, *122*, 214−221.
(31) Pickard, C. J.; Mauri, F. *Phys. Rev. B* **2001**, *63*, 245101.
(32) Clark, S. J.; Segall, M. D.; Pickard, C. J.; Hasnip, P. J.; Probert, M. I. J.; Refson, K.; Payne, M. C. *Z. Kristallogr.* **2005**, *220*, 567−570.
(33) Harris, R. K.; Hodgkinson, P.; Pickard, C. J.; Yates, J. R.; Zorin, V. *Magn. Reson. Chem.* **2007**, *45*, S174−S186.
(34) Ashbrook, S. E.; Le Polles, L.; Pickard, C. J.; Berry, A. J.; Wimperis, S.; Farnan, I. *Phys. Chem. Chem. Phys.* **2007**, *9*, 1587−1598.
(35) Yates, J. R.; Pickard, C. J.; Payne, M. C.; Dupree, R.; Profeta, M.; Mauri, F. *J. Phys. Chem. A* **2004**, *108*, 6032−6037.
(36) Joyce, S. A.; Yates, J. R.; Pickard, C. J.; Brown, S. P. *J. Am. Chem. Soc.* **2008**, *130*, 12663−12670.
(37) Yates, J. R.; Dobbins, S. E.; Pickard, C. J.; Mauri, F.; Ghi, P. Y.; Harris, R. K. *Phys. Chem. Chem. Phys.* **2005**, *7*, 1402−1407.
(38) Webber, A. L.; Emsley, L.; Claramunt, R. M.; Brown, S. P. *J. Phys. Chem. A* **2010**, *114*, 10435−10442.
(39) Webber, A. L.; Elena, B.; Griffin, J. M.; Yates, J. R.; Pham, T. N.; Mauri, F.; Pickard, C. J.; Gil, A. M.; Stein, R.; Lesage, A.; Emsley, L.; Brown, S. P. *Phys. Chem. Chem. Phys.* **2010**, *12*, 6970−6983.
(40) Harris, R. K. *Analyst* **2006**, *131*, 351−373.
(41) *X-AREA and X-RED*; Stoe & Cie: Darmstadt, Germany, 2002.
(42) Sheldrick, G. *Acta Crystallogr., Sect. A* **2008**, *64*, 112−122.
(43) Stejskal, E. O.; Schaefer, J.; Waugh, J. S. *J. Magn. Reson.* **1977**, *28*, 105−112.
(44) Dixon, W. T. *J. Chem. Phys.* **1982**, *77*, 1800−1809.
(45) Metz, G.; Wu, X. L.; Smith, S. O. *J. Magn. Reson., Ser. A* **1994**, *110*, 219−227.
(46) Opella, S. J.; Frey, M. H. *J. Am. Chem. Soc.* **1979**, *101*, 5854−5856.
(47) Bennett, A. E.; Rienstra, C. M.; Auger, M.; Lakshmi, K. V.; Griffin, R. G. *J. Chem. Phys.* **1995**, *103*, 6951−6958.
(48) Marion, D.; Ikura, M.; Tschudin, R.; Bax, A. *J. Magn. Reson.* **1989**, *85*, 393−399.
(49) Hahn, E. L. *Phys. Rev.* **1950**, *80*, 580−594.
(50) Marion, D.; Wüthrich, K. *Biochem. Biophys. Res. Commun.* **1983**, *113*, 967−974.
(51) Vold, R. L.; Waugh, J. S.; Klein, M. P.; Phelps, D. E. *J. Chem. Phys.* **1968**, *48*, 3831−3832.
(52) Robin Bendall, M.; Gordon, R. E. *J. Magn. Reson.* **1983**, *53*, 365−385.
(53) Laasonen, K.; Car, R.; Lee, C.; Vanderbilt, D. *Phys. Rev. B* **1991**, *43*, 6796−6799.
(54) Vanderbilt, D. *Phys. Rev. B* **1990**, *41*, 7892−7895.
(55) Yates, J. R.; Pickard, C. J.; Mauri, F. *Phys. Rev. B* **2007**, *76*, 024401.
(56) Perdew, J. P.; Burke, K.; Ernzerhof, M. *Phys. Rev. Lett.* **1996**, *77*, 3865−3868.
(57) Monkhorst, H. J.; Pack, J. D. *Phys. Rev. B* **1976**, *13*, 5188−5192.
(58) Blatov, V. A.; Shevchenko, A. P.; Serezhkin, V. N. *J. Appl. Crystallogr.* **2000**, *33*, 1193.
(59) Blatov, V. A.; Carlucci, L.; Ciani, G.; Proserpio, D. M. *CrystEngComm* **2004**, *6*, 378−395.
(60) Orellana, G.; Alvarez Ibarra, C.; Santoro, J. *Inorg. Chem.* **1988**, *27*, 1025−1030.
(61) Webber, A. L.; Masiero, S.; Pieraccini, S.; Burley, J. C.; Tatton, A. S.; Iuga, D.; Pham, T. N.; Spada, G. P.; Brown, S. P. *J. Am. Chem. Soc.* **2011**, *133*, 19777−19795.
(62) Szlyk, E.; Lakomska, I.; Kobe, J.; Surdykowski, A.; Glowiak, T.; Sitkowski, J. *Polyhedron* **2002**, *21*, 2001−2007.
(63) Cornago, P.; Claramunt, R. M.; Cano, M.; Heras, J. V.; Gallego, L. M. *ARKIVOC* **2005**, *9*, 21−29.
(64) Harris, R. K., Wasylishen, R. E., Duer, M. J., Eds. *NMR Crystallography*; John Wiley & Sons Ltd.: Chichester, U.K., 2009.
(65) Brouwer, D. H.; Alavi, S.; Ripmeester, J. A. *Phys. Chem. Chem. Phys.* **2008**, *10*, 3857−3860.
(66) Ubbink, M.; Worrall, J. A. R.; Canters, G. W.; Groenen, E. J. J.; Huber, M. *Annu. Rev. Biophys. Biomol. Struct.* **2002**, *31*, 393−422.
(67) Alla, M.; Lippmaa, E. *Chem. Phys. Lett.* **1982**, *87*, 30−33.
(68) Vanderhart, D. L.; Earl, W. L.; Garroway, A. N. *J. Magn. Reson.* **1981**, *44*, 361−401.
(69) Nayeem, A.; Yesinowski, J. P. *J. Chem. Phys.* **1988**, *89*, 4600−4608.

(70) Oldfield, E.; Kinsey, R. A.; Smith, K. A.; Nichols, J. A.; Kirkpatrick, R. J. *J. Magn. Reson.* **1983**, *51*, 325−329.
(71) VanderHart, D. L.; Asano, A.; Gilman, J. W. *Chem. Mater.* **2001**, *13*, 3796−3809.
(72) Bertmer, M.; Wang, M. F.; Krüger, M.; Blümich, B.; Litvinov, V. M.; van Es, M. *Chem. Mater.* **2007**, *19*, 1089−1097.
(73) Ishii, Y.; Wickramasinghe, N. P.; Chimon, S. *J. Am. Chem. Soc.* **2003**, *125*, 3438−3439.
(74) Wickramasinghe, N. P.; Shaibat, M. A.; Jones, C. R.; Casabianca, L. B.; de Dios, A. C.; Harwood, J. S.; Ishii, Y. *J. Chem. Phys.* **2008**, *128*, 052210−15.
(75) Wickramasinghe, N. P.; Shaibat, M. A.; Ishii, Y. *J. Phys. Chem. B* **2007**, *111*, 9693−9696.
(76) Fung, B. M.; Khitrin, A. K.; Ermolaev, K. *J. Magn. Reson.* **2000**, *142*, 97−101.
(77) Detken, A.; Hardy, E. H.; Ernst, M.; Meier, B. H. *Chem. Phys. Lett.* **2002**, *356*, 298−304.
(78) Ganapathy, S.; Chacko, V. P.; Bryant, R. G.; Etter, M. C. *J. Am. Chem. Soc.* **1986**, *108*, 3159−3165.
(79) Chacko, V. P.; Ganapathy, S.; Bryant, R. G. *J. Am. Chem. Soc.* **1983**, *105*, 5491−5492.
(80) Bernheim, R. A.; Brown, T. H.; Gutowsky, H. S.; Woessner, D. E. *J. Chem. Phys.* **1959**, *30*, 950−956.
(81) Blumberg, W. E. *Phys. Rev.* **1960**, *119*, 79−84.
(82) Bourbigot, S.; VanderHart, D. L.; Gilman, J. W.; Awad, W. H.; Davis, R. D.; Morgan, A. B.; Wilkie, C. A. *J. Polym. Sci., Part B: Polym. Phys.* **2003**, *41*, 3188−3213.